Supporting Information for:

Modification and validation of a commercial dynamic chamber for reactive nitrogen and greenhouse gas flux measurements

Moxy Shah¹, Kifle Z. Aregahegn¹, Danial Nodeh-Farahani¹, Leigh R. Crilley^{1,‡}, Tasnia Hasan¹, Yashar Ebrahimi-Iranpour¹, Fahim Sarker¹, Nick Nickerson², Chance Creelman², Sarah Ellis², Alexander Moravek^{1,§}, Trevor C. VandenBoer^{1,*}

¹ Department of Chemistry, York University, Toronto, Ontario, Canada

² Eosense Inc., Dartmouth, Nova Scotia, Canada

[‡] Now at: Atmospheric Services, WSP Australia, Brisbane, QLD, Australia

[§] Now at: German Environment Agency, Department of Air Quality, Dessau-Rosslau, Germany

^{*}Communicating author: tvandenb@yorku.ca

S1. Chamber customized components and LabVIEW software

To meet the performance requirements for measuring N_r gases, chamber modifications were implemented to create inert surfaces that transmit them effectively to downstream gas analyzers. In addition, a reference chamber with an inert surface at the bottom (Figure S1) was required to benchmark the performance of a modified chamber (Figure S2) where fittings and surfaces identified to be reactive or to facilitate stronger surface interactions were replaced with more inert components.

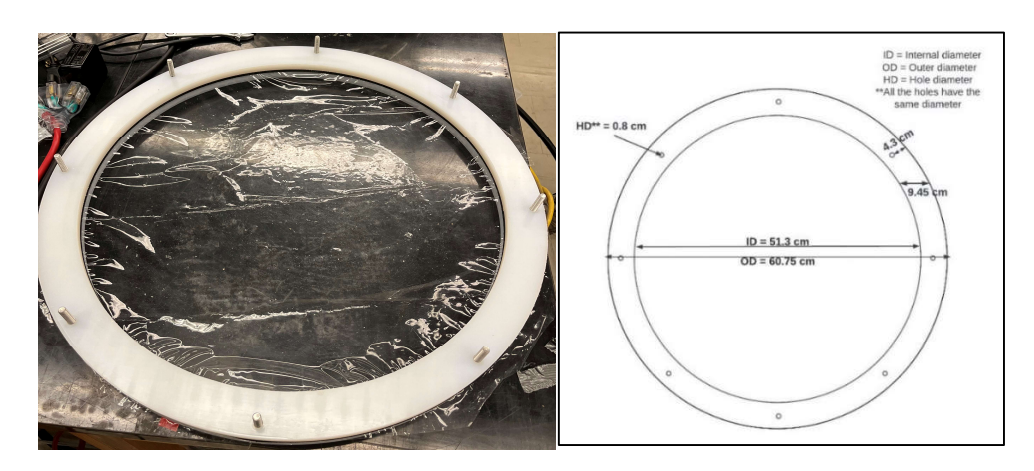


Figure S1. (left) Image of the custom-made base rings made from 1.2 cm thick PTFE with a PFA film pinned between them; all the holes have identical diameters, are located equidistant from the edges of the plate and can fit M8 bolts secured with corresponding nuts (McMasterr-Carr®, PN: 90591A161 and 91263A918). (right) Technical scale drawing of a custom-made ring for the chambers with the inner diameter, outer diameter, ring width, and diameter of holes and their distance from the outer edges denoted.

A custom LabVIEW program was created to automate control of the solenoid valves and mass flow controller in the measurement set up using the microcontroller. The front panel of the LabVIEW program (Figure S3a) allows for the timings of the solenoid valve changes to be manually set, along with the log intervals. A graphical representation of the valve states in real time is also included on the front window to allow for the user to assess the measurement state. In the back window (Figure S3b), the valve timings are controlled within a state machine to allow for continuous valve switching at the time interval selected on the front window. The MFC flow rate is controlled by sending the required voltage to the MFC based on the selected flowrate. The data logging of the valve switching timings and MFC flowrates are handled as well within a state machine to ensure continuous logging to a csv file. The LabVIEW VI is available on the GitHub repository (https://github.com/fjs-vdblab/fluxchamber.git).

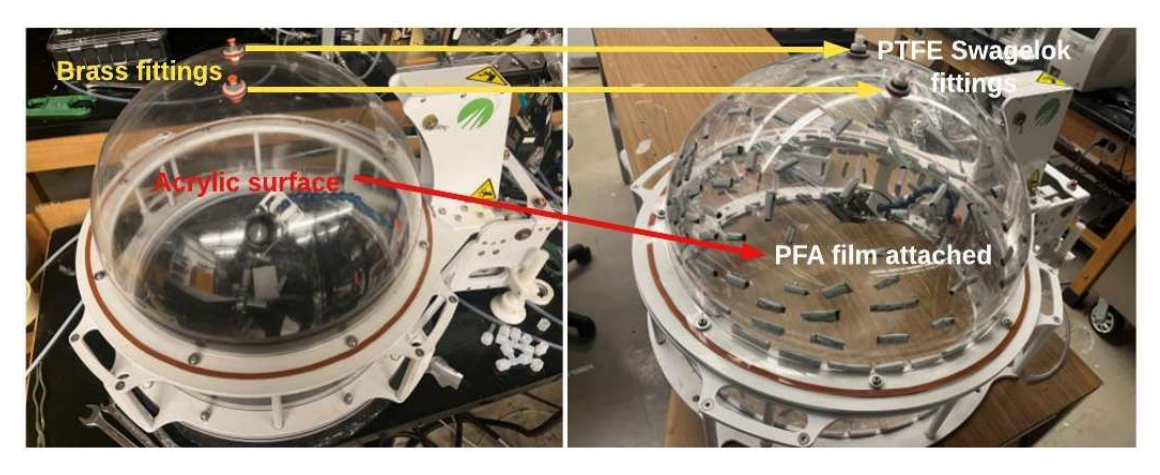


Figure S2. (left) The chamber is in its original configuration from the manufacturer with brass push-connect inlet and outlet fittings and an acrylic dome. (right) The modified chamber with 1/4" PTFE Swagelok bulkhead fittings and an attached film of PFA on the interior of the acrylic dome and all chamber sidewalls using adhesive tape.

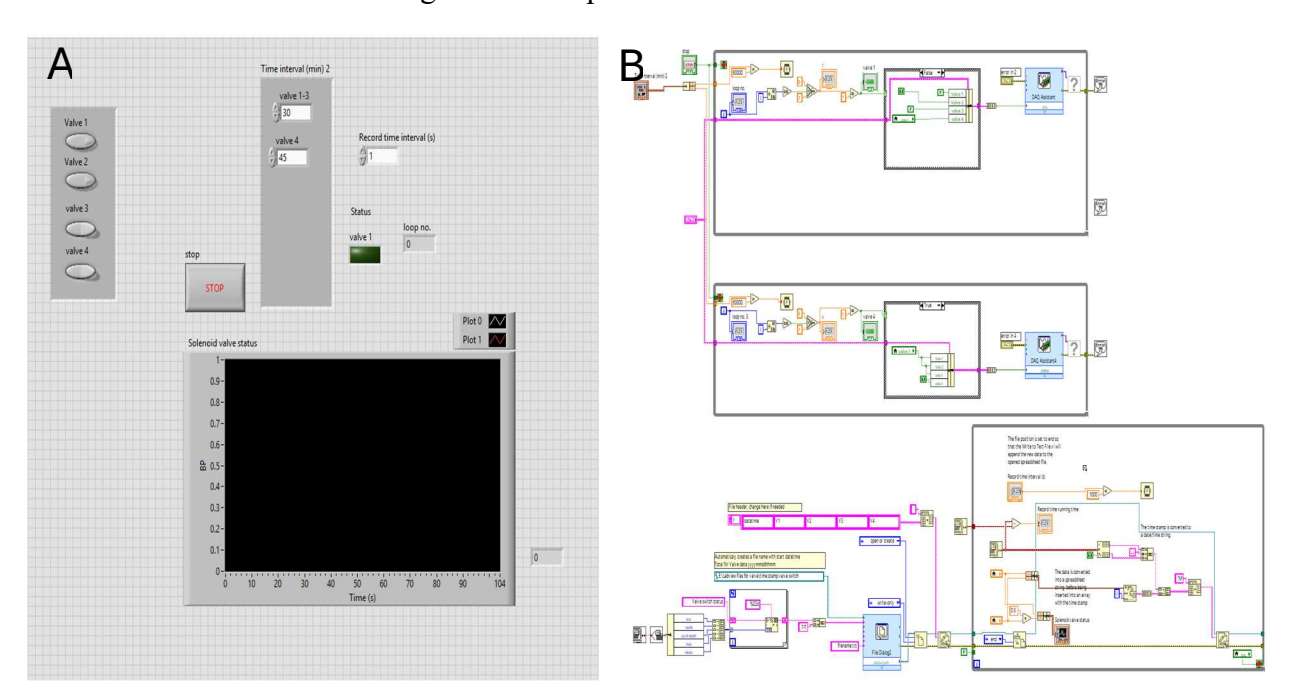


Figure S3. The custom LabVIEW VI for controlling the reference and measurement chambers (A) flows, valve states, timing for lid closures, and rate of datalogging through a graphical user interface front window, and (B) the back window virtual machines controlling the objects, voltages, and data flows.

S2. Gas analyzer quality control procedures

The NO_x analyzer is calibrated with multipoint NO and NO₂ mixing ratios to generate calibration curves on at least an annual basis, with span checks and blanks performed regularly prior to the collection of experimental data. For field use, a full calibration is performed prior to relocation of the system to the deployment site, a span check on site, and again at the end of the deployment

period to account for any instrumental drift. Zero air from a gas-calibration instrument (Gascal 1100TS, American Ecotech, Warren, RI) is introduced to the analyzer through the sampling inlet to set the zero point. If the NO, NO₂ and NO_x readings are within ± 0.5 ppbv of one another, the zero offset is calculated and applied. Then, an NO span check is performed using a known mixing ratio from a certified cylinder (e.g. Praxair, NI NO5MC-A3, 4.88 (± 5 %) ppmv, Toronto, ON) to ensure the NO and NO_x readings are within ± 1 ppbv of the true value. Next, a multi-point precision check of NO is performed at 40 ppbv, 60 ppbv, and 80 ppbv for 30 min, ensuring a stable signal has been achieved. The calibration is considered successful when the analyzer's response to changes in NO mixing ratio is linear, with a slope of 1.00 ± 0.02 and $R^2 > 0.98$. For multi-point precision checks of NO₂, 40 ppbv, 60 ppbv, and 80 ppbv were produced using gas-phase titration of excess NO with O₃, again using the GasCal. The criteria for a successful calibration are the same as described for NO. Conversion efficiency (CE) of NO₂ to NO in the analyzer is the final parameter to be quantified, and a CE > 96% indicates that the molybdenum catalyst in the analyzer is operating reliably.

Calibration for the O_3 analyzer involves a multipoint check, after one hour of warmup time to ensure lamp stability, using 100, 200, 300, and 400 ppbv mixing ratios. The procedure is considered successful if the slope falls between 0.98 and 1.02, the y-intercept between -2 and 2 ppb, and an overall $R^2 > 0.99$.

The calibration and precision check procedure for the Picarro G2509 involved measuring multiple known concentrations of GHGs from a calibration cylinder. The calibration cylinder contained a custom blend of GHGs (4.30 ppm (±5%) N₂O, 24.8 ppm (±5%) CH₄, 3587 ppm (±2%) CO₂), which was a certified standard grade in an air matrix (Linde Canada Plc; PN: AI CD.4MN1C-A3; CGA-590). Pure nitrogen and three calibration points at none, 4.5, and 10-times dilution of the original GHG mixing ratios in the cylinder were delivered to the Picarro analyzer until stable responses were achieved, in triplicate. The dilution of gases was achieved by combining the flow from a liquid N₂ dewar (Linde Canada Plc, PN: NI LC250-230). The observed versus returned slopes of 0.99 for N₂O, 0.99 for CH₄, and 0.98 for CO₂ when compared to the known concentrations delivered, thereby demonstrating suitable and stable calibration of the instrument, as these slopes are within the cylinder mixing ratio uncertainties.

S3. Gas handling for chamber filling and emptying challenge experiments

Dilution and analyte gas flow rates were controlled using MFCs (10 L min⁻¹, PN: 1179C01314CR1BV, MKS instruments Inc, Andover, MA, US). Mixing ratios of CO₂, CH₄ and N₂O were controlled by dilution of a calibration gas cylinder containing a custom blend of the three gases (4000 ppm CO₂, 20 ppm CH₄, 3.3 ppm N₂O in zero air from Linde Canada). Known concentrations of NO and NO₂ were added from their respective calibration gas cylinders (5.9 (±5 %) ppmv of NO in air, PN: NI NO5MC-A3; 4.5 (±5 %) ppmv NO₂ in air, PN: NI NX5MC-AQ; Linde Canada plc, Toronto, ON). Production of known mixing ratios of O₃ to the chamber was achieved by combining output from the built-in ozone generator and photometer of the GasCal into dilution gas at 2 L min⁻¹.

Nitrous acid (HONO) was generated using our in-house calibration source based on the reaction between gas-phase hydrochloric acid (HCl) and a NaNO₂ crystalline film on the surface of PFA tubing (RS-1) at 50% RH to generate gas-phase HONO (Lao et al., 2020).

$$NaNO_{2(s)} + HCl_{(g)} \rightarrow HONO_{(g)} + NaCl_{(s)}$$
 RS-1

In the HONO calibration source, a flow of dry carrier gas (Air Ultra Zero, 99.999%, AI 0.0UZ-K, Praxair) at 50 cm³ min⁻¹ passes through a permeation device (PD) containing HCl solution, heated to 30-40 °C. Another 50 cm³ min⁻¹ passes through a glass impinger containing deionized water to become saturated with water vapour, so the flow obtains an RH of 50% when combined with that of the HCl. This HCl-water vapour mixture enters a NaNO₂-coated PFA reaction device, and HONO is released by acid displacement. The 100 cm³ min⁻¹ flow of HONO exiting the calibration source was diluted using ZA at 2 L min⁻¹, and a mixing ratio of 10-100 ppbv was obtained.

The custom-built permeation oven was also used to generate known mixing ratios of NH₃ by quantification of bubbler-scrubbed NH₃ using ion chromatography (Salehpoor and VandenBoer, 2023). A dry 90 cm³ min⁻¹ zero air flow was passed over a PD containing NH₄OH (30% v/v in 1/8" OD tubing with a 9 cm length). The output was diluted with 2 L min⁻¹ of zero air to generate NH₃ mixing ratios on the order of 30 ppbv.

The time response of gases for the fill and empty process was calculated from the time required to fill the chamber and completely empty the chamber (Figure S4). It can be described by a single exponential function for non-reactive gases such as N₂O, CH₄, CO₂, and NO and thus the time

response, τ , for the exchange of sample gases volume (Section 2.1; E1-4). The double exponential function was used for surface-sensitive and reactive gases, such as NO₂, HONO, and NH₃ to yield two time constants, τ_1 and τ_2 , the time response towards the exchange of the sample air volume and wall interactions (ES-1), respectively (Ellis et al., 2010).

$$f(t) = y_0 + A_1 \times \exp\left(\frac{-(t - t_0)}{\tau_1}\right) + A_2 \times \exp\left(\frac{-(t - t_0)}{\tau_2}\right)$$
 ES-1

Where t_0 is the start time and y_0 is the offset that represents the measurement baseline level; A_1 and A_2 are proportionality coefficients from the contribution of the physical processes of sample volume exchange in the chamber, and reaction and wall interactions, respectively. The relative role of wall interactions or reactions, D, to the overall transfer of gases through a handling system is determined by the contribution of the A_2 term to the sum of both A terms (ES-2).

$$D = \left(\frac{A_2}{A_1 + A_2}\right) \times 100\%$$
 ES-2

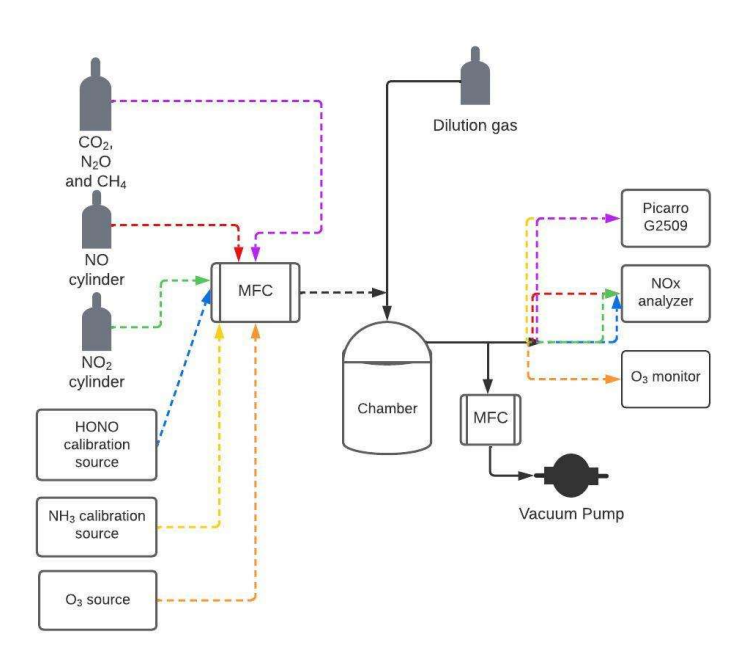


Figure S4. Experimental setup to perform fill/empty experiments in the chambers with greenhouse gases: CH₄, CO₂ and N₂O (purple); N_r gases NO (red), NO₂ (green), HONO (blue), NH₃ (yellow), and O₃ (orange); and dilution gas (black). Dashed arrows show the flow of gases from their respective sources for filling experiments to their respective gas analyzers. Emptying experiments use dilution gas alone once a steady state of the challenge gas has been obtained in the chamber.

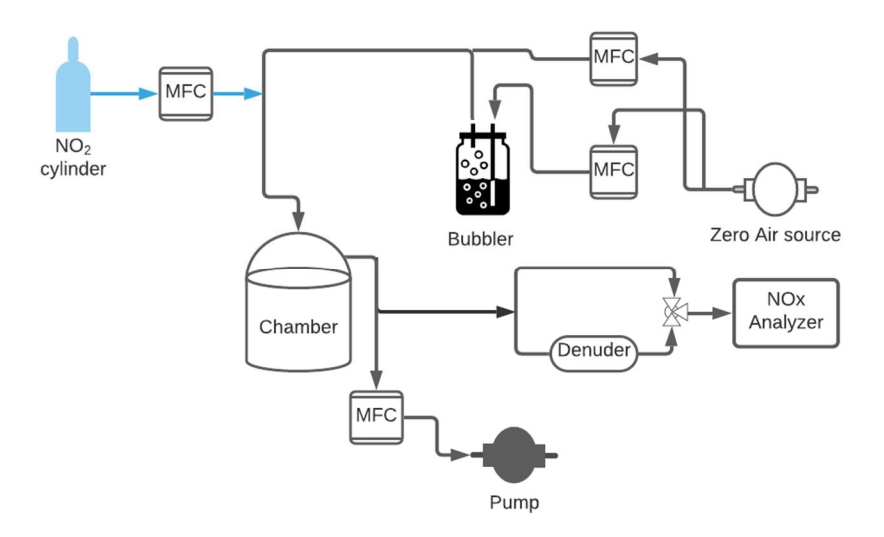


Figure S5. Experimental setup for NO_2 surface loss characterization, where arrows indicate direction of gas flows. Characterization of losses or transformation to HONO was made by a modified NO_x analyzer with experimental flow balance by an added MFC and pump.

S4. Multiplexer modification tests on gas transfer of N_r and GHGs

A 2 L min⁻¹ flow of dry zero air containing 0.058 ppm of N₂O, 0.57 ppm of CH₄, and 81.5 ppm of CO₂, was passed through a multiplexer equipped with either PTFE or stainless-steel (SS) valves and fittings for 30 min to access relative losses. A separate experiment was performed with 2 L min⁻¹ zero air containing a known concentration of NH₃ (0.41 ppm), which was generated based on the method described in Crilley et al. (2023) from a permeation tube containing NH₄OH. Similarly, the transfer efficiency of NO₂ was determined using a calibration cylinder (Linde Canada; PN: NI NX5MC-AQ; 5.9 (±5%) ppm) which was combined with a 2 L min⁻¹ dilution flow of dry ZA to achieve a mixing ratio of 54 ppb. All challenge gases were passed through the multiplexer equipped with either PTFE or SS valves and PFA or SS fittings, respectively, to assess relative losses. All delivered and exiting flows were confirmed to be equal during these tests, ensuring no leaks led to a measured loss. The loss percentage in SS fittings and gas handling valves was measurable but generally remained below 20%, except for NH₃, which exhibited a 38% reduction. With the modifications, minimal surface loss of GHGs and NO₂ (<1%) was observed when using the PFA fittings and PTFE valves, whereas NH₃ exhibited a reduced 11% loss (Figure S6).

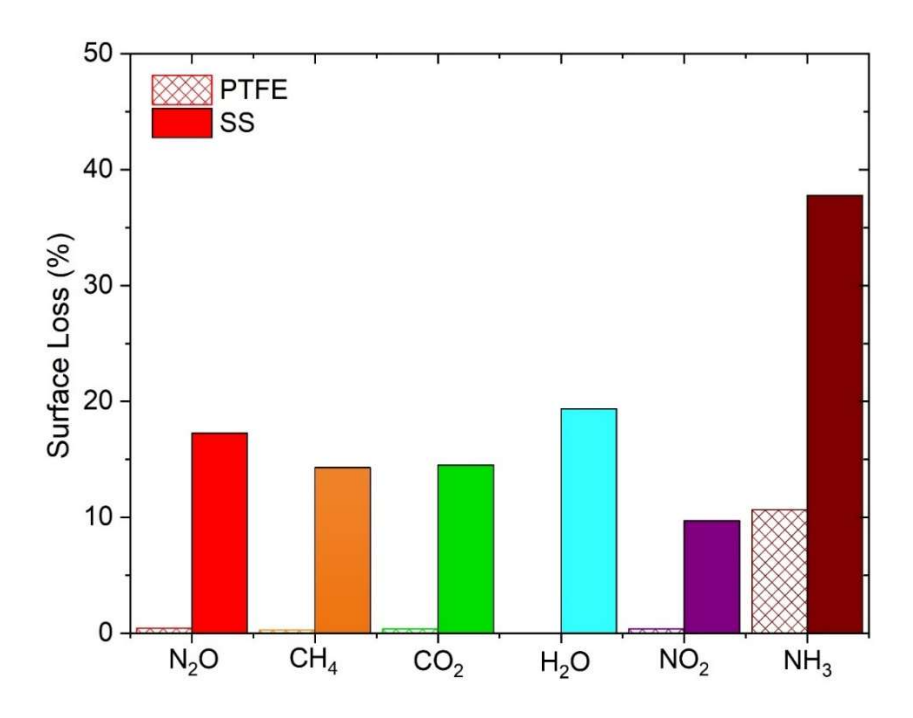


Figure S6. Loss percentage of GHGs (N_2O , CH_4 , CO_2 ,) and N_r (NO_2 , NH_3) gases on stainless steel fittings than that of a PTFE valve and unions.

The surface porosity of SS can influence its adsorption capacity for CH₄ through van der Waals interaction potentials (Sapag et al., 2010). Previous studies have shown that passivation of the SS surface via NO treatment can remove surface iron and promote the formation of chromium-enriched oxide films, which in turn govern the surface chemical reactivity toward NO (Ma et al., 2020). Furthermore, thin layers of iron oxides formed on SS surfaces can affect the interaction with N₂O and alter its decomposition pathways. Consequently, the combined effects of SS surface porosity on CH₄ van der Waals interactions, chromium-oxide passive films influencing NO reactivity, and iron-oxide layers acting as active adsorption sites for N₂O may contribute to up to a 20 % loss of these gases on SS surfaces. It is likely that the surface losses observed here for very clean SS purged extensively with dry zero air prior to these experiments is passivated over time when exposed to ambient air continuously, where the surface adsorption sites are fully occupied and losses no longer occur.

S5. Chamber modification impacts on gas transfer of NO₂

Gas interactions on chamber surfaces during challenge experiments were reversible for all N_r and GHGs tested, except NO₂, which showed reactive losses. These were characterized by calculating

the lost fraction from a small 5 ppb mixing ratio delivered into an unmodified chamber at a high relative humidity of 83%, followed by modifications to reduce this outcome under these challenging simulated environmental conditions (Figure S5). Replacement of the brass push-to-connect fittings delivered the greatest reduction in reactive losses of NO₂, with modest gains obtained from covering chamber surfaces with the PFA film (Figure S7). The final lost fraction of NO₂ in the modified system reported here is technically at the modified NO_x analyzer detection limit and therefore represents a conservative upper limit estimate.

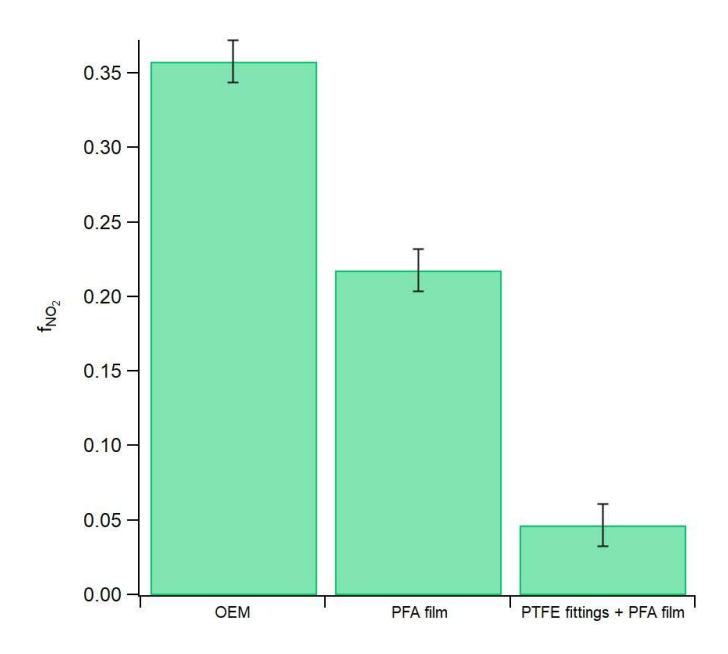


Figure S7. Average NO₂ loss fraction observed upon addition of 5 ppbv of NO₂ at 83% RH to an eosAC-LT® chamber (n = 3 each). These trials were conducted in chambers sequentially: without any modifications (original equipment manufacturer; OEM), following attachment of a PFA film to the inner surface (PFA film), and replacing brass-lined push to connect fittings with ¼" PTFE Swagelok bulkhead (PTFE fittings + PFA film).

S6. Agricultural soil samples used for laboratory N_r emission measurements

A systematic method was used to collect soil samples from an agricultural field to avoid sampling bias, assuming there is no topographic reason for differences in soil properties and nutrient content within the specified plot area. The total field area was divided into eight identical plots (A-H) of $10,800 \,\mathrm{m}^2$ ($120 \,\mathrm{m} \times 90 \,\mathrm{m}$). Soil samples were collected from four random coordinates within each plot, assuming that samples collected within $1 \,\mathrm{m}^2$ were homogeneous. An approximate $1 \,\mathrm{L}$ soil core $\sim 15 \,\mathrm{cm}$ deep was collected with a clean shovel into a pre-labelled clean Ziploc bag. All soil samples were stored below $10 \,\mathrm{^{\circ}C}$ and transported to the laboratory within a week.

Four within-plot samples were collected to better approximate soil properties and nutrient content across the entire field. A total of 32 soil samples were collected from the field, where three of the randomly collected within-plot samples were combined generate a plot scale sample, and one sample within each plot was randomly selected to be combined into a pooled sample representative of the field scale. For the purposes of this work, we assessed the emissions of NO, NO₂, and HONO from duplicate pooled samples and from Plot D within this sampling experiment (Figure S8).

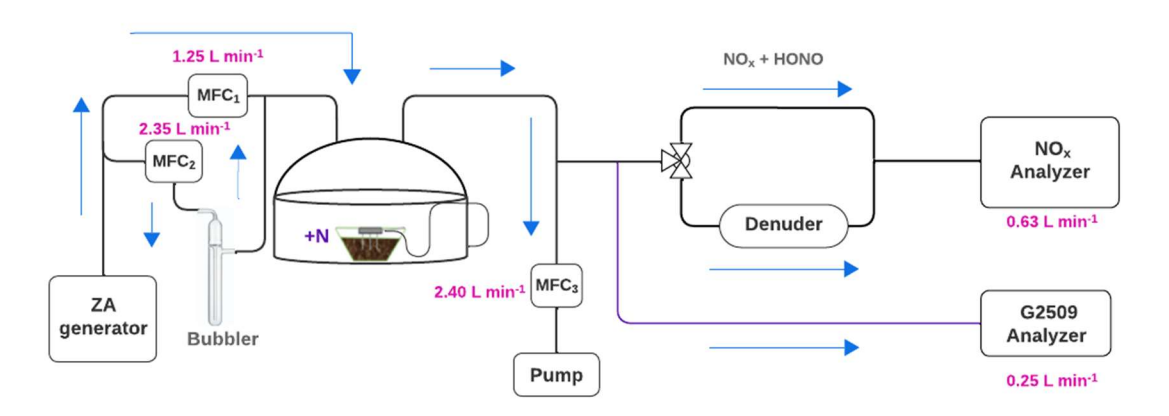


Figure S8. Schematic representation of a dynamic chamber system to measure NO, NO₂, and HONO fluxes with a modified NO_x analyzer (black lines) and NH₃ and N₂O for soil amended with fertilizer using G2509 (purple line). Zero air and humid airflow rates were set using MFC 1 and MFC 2, for a total of 3.6 L min⁻¹ going into the chamber. The three-way valve either sends headspace air directly to the NO_x analyzer (measures NO and NO₂+HONO), or via the Na₂CO₃-coated denuder (measures NO, and NO₂). Blue arrows indicate the flows throughout the experimental setup, with flow rates provided in pink text.

Soil NH₃ and N₂O, along with NO, NO₂, and HONO, were measured when the pooled soil sample was amended with four different nitrogen salts (i.e., AN, urea, ABC, AC; Table S1, Figure 4). For each experiment, 350 g of soil was used, and a corresponding fertilizer solution equivalent to 100 kg N ha⁻¹ was added. Additional experimental details are provided in Section 2.6.1 of the main manuscript. The interpretation of the full set of experimental results will be presented in a forthcoming publication on field-scale heterogeneity of N_r emissions and comments on the assumption that individual samples represent these processes across fields with similar physicochemical properties.

Table S1. The average and integrated flux for soil treated with 4 different nitrogen salts (urea, ammonium bicarbonate (ABC), ammonium carbonate (AC), and ammonium nitrate (AN)). Average fluxes were calculated over the entire experimental cycle. Integrated fluxes were obtained using the trapezoidal rule. Standard deviations reflect the variability in fluxes measured across the time points for the single sample analyzed per treatment. Replicates of urea (~40 hours) and AN (~5 hours) were analyzed with only the modified NO_x analyzer, thus lacking data for N₂O and NH₃ (represented by -).

Soil sample	Avg Flux (μg N m ⁻² hr ⁻¹)					Integrated flux (μg N m ⁻²)				
	NO	NO_2	HONO	N ₂ O	NH ₃	NO	NO_2	HONO	N_2O	NH ₃
Urea	0.1 ± 0.06	0.03 ± 0.01	0.002 ± 0.004	9 ± 3	1 ± 0.5	230	120	1	32400	3700
ABC	0.03 ± 0.01	0.1 ± 0.01	0.03 ± 0.02	7 ± 6	20 ± 7	90	300	90	25300	85900
AC	0.03 ± 0.004	0.2 ± 0.03	0.01 ± 0.01	3 ± 2	20 ± 3	90	500	1	9600	63700
*AN	1 ± 0.1	1 ± 0.1	1 ± 0.02	-	-	50	50	40	-	-

S7. Analytical solutions to soil reactive gas flux determination with a two-chamber setup

For a single chamber system, ES1 can be used to calculate the flux of gases to and from an enclosed surface. Each of these terms and their units are provided in Section 2.7 of the main manuscript.

$$V^{\frac{dC_{\text{cham}}(t)}{dt}} = (A \cdot F_{\text{soil}}(t)) + (Q_{\text{in}} \cdot c_{\text{in}}(t)) - (Q_{\text{out}} \cdot c_{\text{out}}(t)) + (V \cdot R(t))$$
ES1

In our field pilot study, the measurement and reference chambers were installed on clay soil using serrated collars inserted about 10 cm deep into pre-dug circles (30 cm diameter, 20 cm depth) between crop rows of senescing soybeans after removing debris. Collars were left to settle for over 24 h before the chambers were bolted securely to ensure a gas-tight seal. Flux observations were made for two weeks from 02-16 September 2022, during a period when daytime air temperatures were regularly over 25 °C and there were no instances of rain. During the second week of observations, a fertilizer addition of 25 kg N ha⁻¹ was made by broadcasting urea in the chamber, followed by applying clean water to simulate 2.5 cm (1") of rainfall.

In our sampling setup, there is a negligible concentration of any target gas in the inflow $(c_{\rm in}(t)\approx 0)$ due to the use of ultra-pure zero air or nitrogen, and the air is actively mixed inside the chamber with its fan, such that $c_{\rm chamb}=c_{\rm out}$, so the equation simplifies to ES2. For non-steady-state conditions, where the concentration inside the chamber is changing over time, the time-varying nature of the sources and sinks needs to be accounted for. The instantaneous equation that describes the behaviour over an interval $[t_1, t_2]$ is the integral in ES3.

$$V^{\frac{dC_{\text{cham}}(t)}{dt}} = (A \cdot F_{\text{soil}}(t)) - (Q_{\text{out}} \cdot C_{\text{cham}}(t)) + (V \cdot R(t))$$
ES2

$$\int_{t_1}^{t_2} V \frac{dC_{\text{cham}}(t)}{dt} dt = \int_{t_1}^{t_2} [(A \cdot F_{\text{soil}}(t)) - (Q_{\text{out}} \cdot C_{\text{cham}}(t)) + (V \cdot R(t))] dt$$
 ES3

Assuming the soil flux, $F_{\text{soil}}(t)$ (mol m⁻² s⁻¹), is constant over the time interval [t₁, t₂] is a reasonable assumption for experimental setups where the environmental conditions and, where relevant, soil-plant activity, do not change substantially over short periods of a few to tens of minutes (Pape et al., 2009). Rearranging the ES3 expression, a flux can be calculated using ES4.

$$F_{soil} = \frac{V\Delta C_{\text{cham}} + Q_{\text{out}} \int_{t_1}^{t_2} c_{\text{cham}}(t) dt - V \int_{t_1}^{t_2} R(t) dt}{A(t_2 - t_1)}$$
ES4

The volumetric mixing ratio (ES5) is often the unit of measurement for many gas analyzers and defined as the number of moles of the gas divided by the number of moles of dry air. The mixing ratio X is dimensionless and provides a way to express gas concentrations independently of changes in temperature or pressure.

$$X = \frac{n_{\text{gas}}}{n_{\text{air}}}$$
 ES5

We can then write the molar concentration, c (mol m⁻³), in the form of volumetric mixing ratio using ES6:

$$c_{\text{chamber}} = X_{\text{out}} \times \rho_d$$
 ES6

Here, ρ_d (mol m⁻³) is the molar density of the air. The total pressure P is equal to atmospheric pressure, such that by using the ideal gas law, we can define the density of air using ES7:

$$\rho_d = \frac{P}{R \cdot T}$$
 ES7

Where, P (Pa) is the pressure, R (J mol⁻¹ K⁻¹) is the universal gas constant, and T (K) is the absolute temperature. In ES7 it is assumed that atmospheric air behaves as an ideal gas, which is a reasonable approximation under typical environmental conditions, even at the Earth's surface. The resulting molar concentrations can then be calculated and used in the flux determinations as presented in E6 and E7 in the main manuscript.

S7.1 Dynamics and physical corrections from reference and measurement chambers

In environmental and experimental settings where gas flux is measured, it is important to capture the rate at which gas concentrations change over time. This rate reflects the net outcome from both gas emission and deposition occurring simultaneously, influenced by the surface under study, temperature, pressure, flow, and surface interactions (ES8). The RC (r), which operates under identical conditions to the MC (m) but excludes the surface under study by isolating it beneath the PFA film, takes into account the environmental and surface effects, such that its observed flux rate is described by (ES9). To isolate the effects of the surface under study from reactions taking place in the atmospheric sample and on the chamber surfaces, the rate of change in the RC is subtracted from that in the MC, yielding the net flux through ES10.

$$F_{\rm m} = {
m surface} \ {
m under} \ {
m study} + {
m environmental} \ {
m and} \ {
m chamber} \ {
m effects}$$

$$ES9$$

$$F_{\rm net} = F_{\rm m} - F_{\rm r}$$

$$ES10$$

The net rate of change can now be used to calculate the molar flux by substituting it into ES4 to arrive at ES11, which is the core of E6.

$$F_{\text{net}} = \frac{V}{A} \left(\frac{\Delta C_m}{\Delta t_m} - \frac{\Delta C_r}{\Delta t_r} \right) + \frac{Q_{\text{out}}}{A} \left(\frac{\int_{t_{1m}}^{t_{2m}} c_m(t) \ dt}{\Delta t_m} - \frac{\int_{t_{1r}}^{t_{2r}} c_r(t) \ dt}{\Delta t_r} \right)$$

$$- \frac{V}{A} \left(\frac{\int_{t_{1m}}^{t_{2m}} R_m(t) \ dt}{\Delta t_m} - \frac{\int_{t_{1r}}^{t_{2r}} R_r(t) \ dt}{\Delta t_r} \right)$$
ES11

The closure period of the two chambers is matched to facilitate an accurate correction of the kinetics and surface interactions. The calculated flux from the surface under study is therefore corrected for background and environmental effects, reducing systematic bias from gas reactivity.

Last, we introduce a flux loss factor (λ ; ES12) to correct for partial transmission of a targeted reactive gas due to adsorption to chamber walls and gas handling lines during a measurement cycle (t_1 - t_2). This factor needs to be determined empirically through calibration experiments, like those presented in Figure 2, where the loss is quantified relative to theoretical expectations for each gas of interest during both filling and emptying processes.

$$\lambda = \frac{\int_{t_1}^{t_2} \left(\frac{dX}{dt}\right)_{theoretical} dt}{\int_{t_1}^{t_2} \left(\frac{dX}{dt}\right)_{measured} dt}$$
ES12

We can account for λ in ES11, to get the molar flux of gas inside the chamber, which accounts for flux loss (ES13) by scaling the equation directly to arrive at the full form presented as E6 in the main manuscript.

$$F_{\text{net}} = (\lambda) \cdot \left(\frac{V}{A} \left(\frac{\Delta C_m}{\Delta t_m} - \frac{\Delta C_r}{\Delta t_r} \right) + \frac{Q_{\text{out}}}{A} \left(\frac{\int_{t_{1m}}^{t_{2m}} c_m(t) \ dt}{\Delta t_m} - \frac{\int_{t_{1r}}^{t_{2r}} c_r(t) \ dt}{\Delta t_r} \right) \right)$$

$$- \frac{V}{A} \left(\frac{\int_{t_{1m}}^{t_{2m}} R_m(t) \ dt}{\Delta t_m} - \frac{\int_{t_{1r}}^{t_{2r}} R_r(t) \ dt}{\Delta t_r} \right) \right)$$
ES13

S7.2 Chemical corrections from reference and measurement chambers

For reactive species impacting our N_r suite – mainly NO, O_3 , and NO_2 – flux values can be attenuated or enhanced due to the reaction of NO with O_3 (RS-2). We show below (Figure S9) that the photolysis of NO_2 and HONO are negligible due to the high-energy photon cut-off of acrylic (<400 nm threshold) (RS-3). Nevertheless, we include the NO_2 photolysis term in the rate expression for completeness, noting that under our field conditions its contribution (Section S7.2.1) is within the noise of the NO_2 fluxes. The rate of RS-2 and RS-3 for NO_2 , therefore, can be expressed by ES14.

$$NO + O_3 \rightarrow NO_2 + O_2$$
 RS-2

$$NO_2 + hv \rightarrow NO + O$$
 RS-3

$$\frac{d[NO_2]}{dt} = k_{NO+O_3}[NO][O_3] - J_{NO_2}[NO_2]$$
 ES14

The total change in the concentration due to reaction over a cycle can be expressed by integrating the rate equation over the cycle duration, as the start time (t_0) and end time (t) are known, therefore replacing the term R in ES13 (and E6) with the expression in ES15. Under our chamber conditions, the integrated photolysis contribution was smaller than the measurement uncertainty of the NO₂ fluxes (Section S7.2.1), and therefore it was not included as an explicit term in ES15.

$$\int_{t_0}^{t} R \ dt = \Delta[NO] = \Delta[O_3] = -\Delta[NO_2] = -\int_{t_0}^{t} k [NO(t)][O_3(t)] \ dt$$
ES15

Where the R is the loss rate due to the reaction for NO and O₃ ($R \le 0$) and simultaneous production rate for NO₂ ($R \ge 0$). For the kinetic determination, number density of the gases (molec cm⁻³) are used to track the chemical transformations over time, but instrumentation typically measures mixing ratios. If temperature and pressure are measured alongside target gases in the dynamic chambers, then using ES6 and ES7, the reaction-corrected flux based on measured mixing ratios can be calculated using ES16.

$$F_{\text{net}} = \lambda \cdot \frac{P_{\text{air}}}{R \cdot T} \cdot \left(\frac{V}{A} \left(\frac{\Delta X_m}{\Delta t_m} - \frac{\Delta X_r}{\Delta t_r} \right) + \frac{Q_{\text{out}}}{A} \left(\frac{\int_{t_{1m}}^{t_{2m}} X_m(t) \ dt}{\Delta t_m} - \frac{\int_{t_{1r}}^{t_{2r}} X_r(t) \ dt}{\Delta t_r} \right) - \frac{V}{A} \left(\frac{P_{\text{air}}}{R \cdot T} \right) \left(\frac{\int_{t_{1m}}^{t_{2m}} k \cdot X_{\text{NO}_m}(t) \cdot X_{\text{O3}_m}(t) \ dt}{\Delta t_m} - \frac{\int_{t_{1r}}^{t_{2r}} k \cdot X_{\text{NO}_r}(t) \cdot X_{\text{O3}_r}(t) \ dt}{\Delta t_r} \right) \right)$$

ES16

Where, again, P_{air} (Pa) is the atmospheric pressure inside the measurement and reference chambers, R (J mol⁻¹ K⁻¹) is the gas constant, and T (K) is the temperature inside the RC and MC. For non-reactive gases like CO₂, CH₄, and N₂O, there is no reaction term and the flux can be described simply using ES17 as below, which is presented as E7 in the main manuscript.

$$F_{\text{net}} = \lambda \cdot \frac{P_{\text{air}}}{R \cdot T} \cdot \left(\frac{V}{A} \left(\frac{\Delta X_m}{\Delta t_m} - \frac{\Delta X_r}{\Delta t_r} \right) + \frac{Q_{\text{out}}}{A} \left(\frac{\int_{t_{1m}}^{t_{2m}} X_m(t) \, dt}{\Delta t_m} - \frac{\int_{t_{1r}}^{t_{2r}} X_r(t) \, dt}{\Delta t_r} \right) \right)$$
 ES17

S7.2.1 Losses of NO₂ or HONO due to photolysis within transparent chambers

The fraction of NO₂ or HONO lost due to photolysis depends on the photons transmitted through the chamber material (Figure S9). The photolysis rate is estimated here under a worst-case scenario with respect to our field observations, using actinic flux data collected for Lambton County, Ontario, Canada, at 12:00 PM local time on September 10, 2022, under clear sky conditions. The effective photolysis rate constant within the chamber was calculated to be 2.62 x 10⁻⁴ s⁻¹, using ES18.

$$J = \int [\sigma(\lambda) \cdot \phi(\lambda) \cdot F(\lambda) \cdot T(\lambda)] d\lambda$$
 ES18

Where $\sigma(\lambda)$ is the absorption cross-section of NO₂ (cm² molecule⁻¹), $\Phi(\lambda)$ is the quantum yield (dimensionless; 0-1), $F(\lambda)$ is the actinic flux (photons cm⁻² s⁻¹ nm⁻¹), and $T(\lambda)$ is the transmission of the acrylic chamber material (dimensionless) at wavelength λ (dimensionless; 0-1).

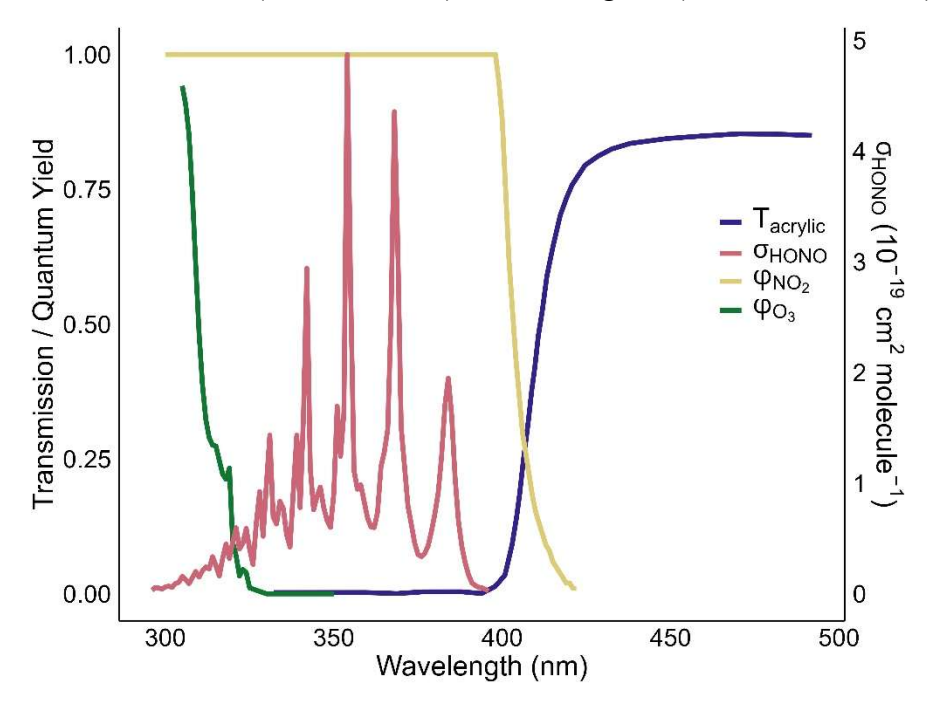


Figure S9. Transmission of light through the chamber and quantum yields for photolysis of O_3 and NO_2 , along with the absorption cross section of HONO, as a function of wavelength. Note the negligible overlap for photodissociation. The acrylic effectively blocks wavelengths below approximately 400 nm, meaning the photolysis rate of NO_2 is the only one impacted by a chamber constructed from this material.

Using this attenuated loss rate in a kinetic model, we find that at most 14% of the initial NO₂ concentration is lost due to photolysis within the chamber in the first 10 minutes, and 37% within 30 minutes (Figure S10, blue trace). This rate of photolysis significantly reduces the NO₂ mixing ratio within the chamber environment. The wavelength cut-off of polyacrylate limits the penetration of shorter wavelengths, which are more effective in driving NO₂ photolysis, so the overall rate is slowed inside the chamber compared to ambient conditions (Figure S10, red trace). Despite this, within the initial 30-minute timeframe (Figure S10, vertical dashed line), the change in the fraction of NO₂ lost is relatively small due to the dynamic nature of the chamber headspace (i.e. due to continuous sampling and dilution flows), allowing for a reasonable linear approximation of the curve. The photolytic loss of HONO is much more impacted by the cutoff wavelength of the polyacrylate chamber lid, to the point where it is not substantially lost due to

photolysis. As shown in Figure S9, the HONO absorption cross-section lies almost entirely below the ~400 nm transmission cutoff of the chamber lid. This spectral mismatch means that HONO photolysis is effectively suppressed inside the chamber, unlike NO₂, which still absorbs within the transmitted range. Consequently, chamber-derived HONO fluxes are not biased by photolytic loss, making their interpretation simpler than NO₂.

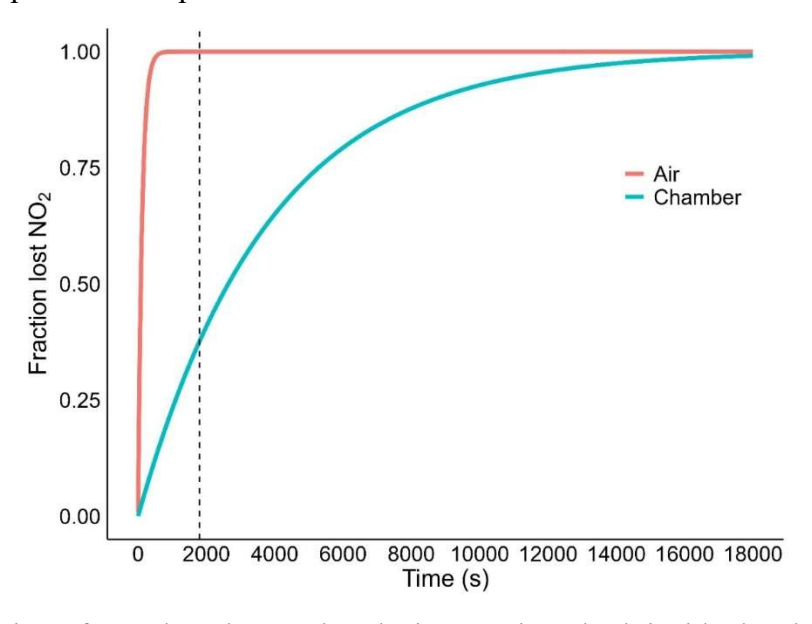


Figure S10. Fraction of NO₂ lost due to photolysis over time, both inside the chamber (blue line) and in ambient air (red line). The vertical dashed line indicates the 30-min mark, where an initial linear approximation of the loss rate can be applied.

This simplification yields an estimated initial photolysis rate loss of approximately 1% per minute for NO₂ over the initial 30-minute measurement cycle and effectively 0% per minute for HONO under chamber conditions due to the cutoff wavelength. This linear approximation is only valid for this kind of short initial period. Beyond 30 minutes, the overall trend exhibits a steeper exponential decay, characteristic of the NO₂ photolysis process. This photolysis contribution is included within the reaction term (ES14). Its effect (~1% min⁻¹ maximum at noon under clear-sky conditions) is smaller than the uncertainties of the NO₂ flux measurements, so it is not explicitly propagated into the flux equations in this work.

S7.3 Surface interaction correction using the attenuation factor (λ)

Accurate quantification of trace gas fluxes using dynamic chamber systems also requires correction for attenuation caused by gas-wall interactions and the associated sensor response delays. These effects can significantly suppress the measured accumulation rate of reactive species

within the closed chamber, particularly for compounds with strong surface affinity, such as NH₃, NO₂, and HONO, requiring the use of the attenuation factor (λ ; ES12).

The attenuation factor is derived from our controlled delivery experiments that simulated two sequential measurement scenarios: a filling phase, where gas is introduced and accumulates within the chamber, and an emptying phase, where the chamber is flushed and the gas signal declines (Figure 4). In an ideal system without wall interactions, the integrated difference between theoretical and observed concentrations within a single chamber should approach zero, and λ would be approximately one. However, as shown in Figure S11, all three gases exhibited surface interactions, with NH₃ showing the largest deviation from theoretical predictions.

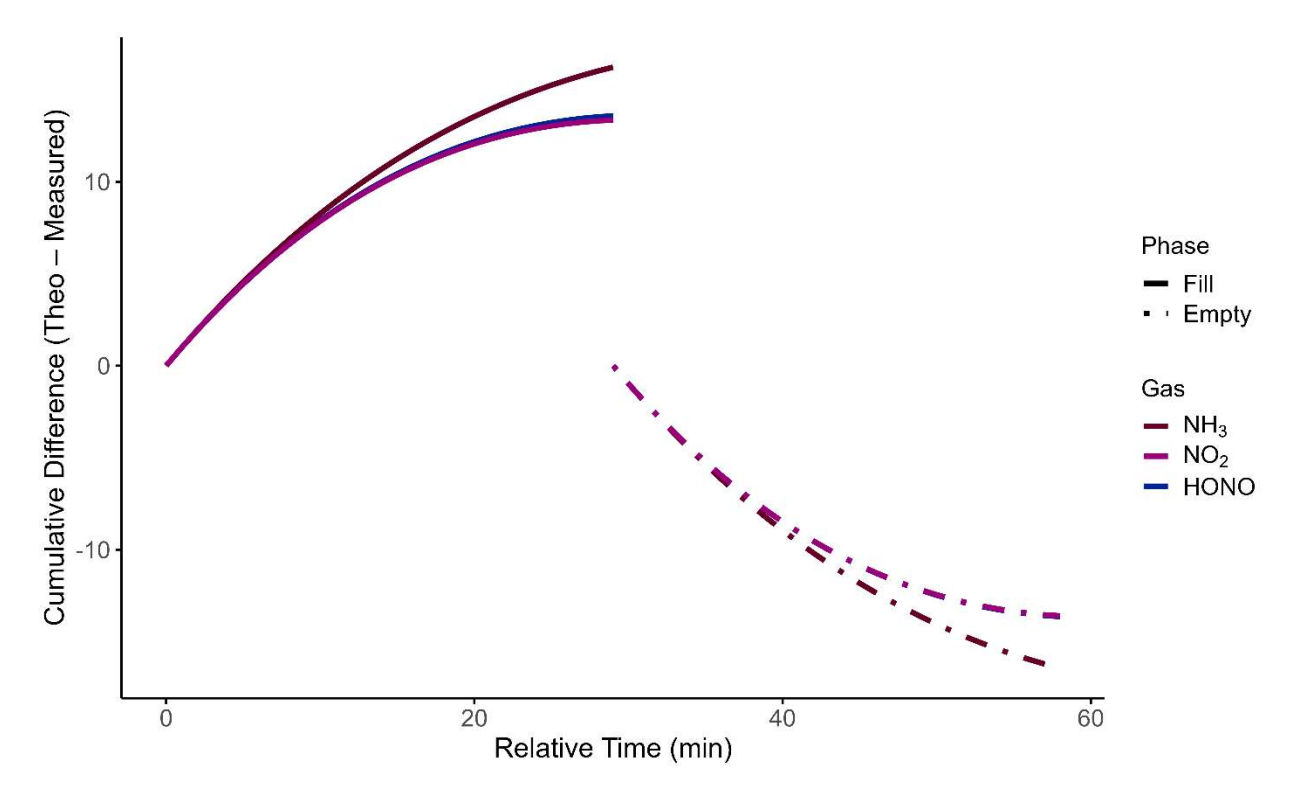


Figure S11. Cumulative integration of the difference between theoretical and measured gas concentrations for NH₃, NO₂, and HONO over a 30-minute filling and emptying period. Theoretical concentrations represent expected values without attenuation, while measured values reflect signal loss due to gas—wall interactions. Solid lines correspond to the filling phase; dashed lines represent the emptying phase, together representing a full in situ measurement cycle. These integrals illustrate the time-dependent and nonlinear attenuation that underlies the empirical calculation of λ .

When filling, the gas accumulates in the chamber, with strong initial attenuation that diminishes over time as the surfaces passivate. Conversely, adsorbed gases from surface passivation may partially desorb during emptying, offsetting some of the losses observed during filling. Two respective λ values can be derived and considered separately by integrating the filling and emptying concentration-time series independently.

Where a single-chamber is used to study an experimental system, the filling- and emptying-phase effects offset one another, masking the attenuation as all the surface interacting molecules are eventually transferred to the gas analyzer. In field applications with a dual chamber approach in use, this symmetry is lost because the measurement chamber accumulates a real emission flux during a defined closure period, while the reference chamber does not. Hence, an empirical calculation of λ is needed which compensates for the attenuation in both the accumulation and depletion of the target gas (Table S7). For NH₃, the fill-phase difference was 16.23, dividing the expected theoretical accumulation by this measured accumulation yields a λ_{fiill} of 5.40, while the empty-phase difference was -16.44, with a λ_{empty} of 0.36. Unsurprisingly, NO₂ and HONO followed a similar trend as we also noted their surface interactions, with λ_{fiill} values of 3.04 and 3.14 resulting from our characterizations, respectively, and λ_{empty} values near 0.40.

From a physical and mathematical standpoint, attenuation reduces all concentration-dependent components of the flux (accumulation/depletion, dilution, and reaction) by the same factor. As a result, the attenuation factor λ scales the entire net-flux expression rather than only the accumulation term.

Table S7. The cumulative integrated differences between theoretical and measured values from Figure S11 for both the filling and emptying phases, and the resulting λ values. While the signed fill and empty values appear approximately balanced, their directional impact differs, and the underlying asymmetry becomes critical in real measurements.

Gas	$\int (\text{Theo} - \text{Meas})_{\text{fill}}$	\int (Theo – Meas) _{empty}	difference	λ_{fill}	λ _{empty}
NH ₃	16.23	-16.33	-0.20	5.40	0.36
NO ₂	13.40	-13.64	-0.23	3.04	0.40
HONO	13.57	-13.65	-0.05	3.14	0.40

S8. References

- Crilley, L. R., Lao, M., Salehpoor, L., & VandenBoer, T. C. (2023). Emerging investigator series: an instrument to measure and speciate the total reactive nitrogen budget indoors: description and field measurements. *Environmental Science: Processes and Impacts*, *25*(3), 389–404. https://doi.org/10.1039/d2em00446a
- Ellis, R. A., Murphy, J. G., Pattey, E., Van Haarlem, R., O'brien, J. M., & Herndon, S. C. (2010). Characterizing a Quantum Cascade Tunable Infrared Laser Differential Absorption Spectrometer (QC-TILDAS) for measurements of atmospheric ammonia. *Atmos. Meas. Tech*, 3, 397–406.
- Lao, M., Crilley, L. R., Salehpoor, L., Furlani, T. C., Bourgeois, I., Andrew Neuman, J., Rollins, A. W., Veres, P. R., Washenfelder, R. A., Womack, C. C., Young, C. J., & VandenBoer, T. C. (2020). A portable, robust, stable, and tunable calibration source for gas-phase nitrous acid (HONO). *Atmospheric Measurement Techniques*, *13*(11), 5873–5890. https://doi.org/10.5194/amt-13-5873-2020
- Ma, L., Pascalidou, E. M., Wiame, F., Zanna, S., Maurice, V., & Marcus, P. (2020). Passivation mechanisms and pre-oxidation effects on model surfaces of FeCrNi austenitic stainless steel. *Corrosion Science*, *167*, 108483. https://doi.org/10.1016/J.CORSCI.2020.108483
- Pape, L., Ammann, C., Nyfeler-Brunner, A., Spirig, C., Hens, K., & Meixner, F. X. (2009). An automated dynamic chamber system for surface exchange measurement of non-reactive and reactive trace gases of grassland ecosystems. *Biogeosciences*, 6(3), 405–429. https://doi.org/10.5194/bg-6-405-2009
- Salehpoor, L., & VandenBoer, T. C. (2023). Suppressor and calibration standard limitations in cation chromatography of ammonium and 10 alkylamines in atmospheric samples. *Analytical Methods*, *15*(31), 3822–3842. https://doi.org/10.1039/d3ay01158e
- Sapag, K., Vallone, A., Blanco, A. A. G., & Solar, C. (2010). Adsorption of Methane in Porous Materials as the Basis for the Storage of Natural Gas. *Natural Gas*. https://doi.org/10.5772/9846